

THE WFC3 INFRARED SPECTROSCOPIC PARALLEL (WISP) SURVEY *

A TEK, H.¹, MALKAN, M.², MCCARTHY, P.³, TEPLITZ, H.I.⁴, SCARLATA, C.¹, SIANA, B.⁵, HENRY, A.⁶, COLBERT, J.W.¹, ROSS, N.R.², BRIDGE, C.⁵, BUNKER, A.J.⁷, DRESSLER, A.³, FOSBURY, R.A.E.⁸, MARTIN, C.⁶, SHIM, H.¹

Draft version August 27, 2018

ABSTRACT

We present the WFC3 Infrared Spectroscopic Parallel (WISP) Survey. WISP is obtaining slitless, near-infrared grism spectroscopy of ~ 90 independent, high-latitude fields by observing in the pure parallel mode with Wide Field Camera-3 on the *Hubble Space Telescope* for a total of ~ 250 orbits. Spectra are obtained with the G102 ($\lambda = 0.8\text{--}1.17\ \mu\text{m}$, $R \sim 210$) and G141 grisms ($\lambda = 1.11\text{--}1.67\ \mu\text{m}$, $R \sim 130$), together with direct imaging in the J- and H-bands (F110W and F140W, respectively). In the present paper, we present the first results from 19 WISP fields, covering approximately $63\ \text{arcmin}^2$. For typical exposure times ($\sim 6400\ \text{s}$ in G102 and $\sim 2700\ \text{s}$ in G141), we reach 5σ detection limits for emission lines of $f \sim 5 \times 10^{-17}\ \text{ergs s}^{-1}\ \text{cm}^{-2}$ for compact objects. Typical direct imaging 5σ -limits are 26.8 and 25.0 magnitudes (AB) in F110W and F140W, respectively. Restricting ourselves to the lines measured with highest confidence, we present a list of 328 emission lines, in 229 objects, in a redshift range $0.3 < z < 3$. The single-line emitters are likely to be a mix of $\text{H}\alpha$ and $[\text{OIII}]\lambda 5007, 4959\ \text{\AA}$, with $\text{H}\alpha$ predominating. The overall surface density of high-confidence emission-line objects in our sample is approximately 4 per arcmin^2 . These first fields show high equivalent width sources, AGN, and post starburst galaxies. The median observed star formation rate of our $\text{H}\alpha$ selected sample is $4\ M_{\odot}\ \text{year}^{-1}$. At intermediate redshifts, we detect emission lines in galaxies as faint as $H_{140} \sim 25$, or $M_R < -19$, and are sensitive to star formation rates down to less than $1\ M_{\odot}\ \text{year}^{-1}$. The slitless grisms on WFC3 provide a unique opportunity to study the spectral properties of galaxies much fainter than L^* at the peak of the galaxy assembly epoch.

Subject headings: galaxies: distances and redshifts – galaxies: statistics – infrared: galaxies – surveys

1. INTRODUCTION

While there is considerable uncertainty regarding the detailed star formation history of galaxies of various masses and types, it has become clear that the span of cosmic time $0.5 \leq z \leq 2.5$ encompasses most of the star formation in the history of the Universe (e.g. Hopkins, A. 2004; Daddi et al. 2007). This broad epoch is also when many galaxies were “assembled,” when major mergers and the accretion of satellite galaxies and gas combined to produce the variety of morphologies and structures of modern galaxies. There is mounting evidence for an evolution of star-forming galaxies during this time period, from high-mass galaxies dominating at $z \sim 3$, to low-mass galaxies at the present. Deep, wide IR surveys are required to cover much of the peak epoch of star formation, because of the redshifting of the key diagnostic spectral features of stellar evolution, and to

minimize the effect of obscuration by dust.

The difficulty of obtaining observed-frame near-infrared spectra causes much of our empirical perspective on galaxy evolution to be biased by the way in which spectroscopic samples are selected. Color selection reliably selects common objects, but misses unexpected ones; magnitude-limited samples necessarily favor bright-continuum objects. Ground-based searches for emission lines from faint high-redshift galaxies are severely impacted by the bright NIR airglow. Excluding OH terrestrial airglow frequencies restricts redshift coverage and compromises redshift identification. Space-based spectroscopic surveys offer significant advantages for unbiased target selection. The grisms on the Near Infrared Camera and Multi Object Spectrometer (NICMOS), the Space Telescope Imager and Spectrograph (STIS) and the Advanced Camera for Survey (ACS) have demonstrated the power of spectroscopy from above the atmosphere, where the low background emission permits slitless observing (Gardner et al. 1998; McCarthy et al. 1999; Teplitz et al. 2003; Pirzkal et al. 2004; Drozdovsky et al. 2005). Furthermore, the terrestrial wavelength gaps can only be filled from space, as first demonstrated by the pure-parallel program with the NICMOS G141 grism (McCarthy et al. 1999; Yan et al. 1999; Shim et al. 2009).

Much as ground-based objective prism surveys (e.g. Gallego et al. 1999) were used to define flux-limited samples of $\text{H}\alpha$ emitters at $z \sim 0$, the NICMOS grism observations produced complete samples of emission-line objects at intermediate redshifts. Yan et al. (1999) and Hopkins et al. (2000) used observations with the NICMOS H-band (G141) grism to derive $\text{H}\alpha$ luminosity functions,

*BASED ON OBSERVATIONS MADE WITH THE NASA/ESA HUBBLE SPACE TELESCOPE, WHICH IS OPERATED BY THE ASSOCIATION OF UNIVERSITIES FOR RESEARCH IN ASTRONOMY, INC., UNDER NASA CONTRACT NAS 5-26555. THESE OBSERVATIONS ARE ASSOCIATED WITH PROGRAM 11696

¹ Spitzer Science Center, Caltech, Pasadena, CA 91125

² Dep’t. of Physics and Astronomy, Univ. of Calif. Los Angeles

³ Observatories of the Carnegie Institution for Science, Pasadena, CA 91101

⁴ Infrared Processing and Analysis Center, Caltech, Pasadena, CA 91125

⁵ Department of Astronomy, Caltech, Pasadena, CA 91125

⁶ Dep’t. of Physics, Univ. of Calif. Santa Barbara, CA 93106

⁷ Department of Physics, University of Oxford, Denys Wilkinson Building, Keble Road, OX13RH, U.K.

⁸ Space Telescope - European Coordinating Facility, Garching bei München, Germany

and to show that the luminosity density, and hence star formation rate density, has evolved by a factor of ~ 10 from $z \sim 1.4$ to the present. Shim et al. (2009) used a larger sample to derive improved $H\alpha$ luminosity functions in two redshift bins and confirmed the trends seen in the analysis by Yan et al. and Hopkins et al. The complete reductions/extractions of grism data for the principal modes of NICMOS were released in the Hubble Legacy Archive (HLA, Freudling et al. 2008). Nearly all of the published results from the NICMOS grisms were based on data with the G141 H-band disperser. The poor sensitivity of the NICMOS detector at short wavelengths limited the utility of the J_110-band grism.

The grisms on ACS have been used to discover faint $Ly\alpha$ emission sources and faint Lyman continuum break sources at $z \sim 3 - 4$ (Malhotra et al. 2005; Pirzkal et al. 2007) as well as to derive spectrophotometric redshifts for a large sample of faint galaxies (e.g. Straughn et al. 2008, 2009). Extremely deep ACS grism observations have shown the power of low resolution spectroscopy above the atmosphere to detect spectral breaks indicative of passively evolving systems (e.g. Daddi et al. 2005) or active star forming galaxies (Pirzkal et al. 2004; Rhoads et al. 2005; Malhotra et al. 2005; Pasquali et al. 2006). The full release of the reduced ACS grism data in the HLA is underway (Kuemmel et al. 2009b). The STIS slitless modes work at higher resolution than the NICMOS and ACS grisms, but the relatively low sensitivity of STIS has limited its ability to sample populations beyond the reach of ground-base spectroscopic surveys (Teplitz et al. 2003).

Wide Field Camera Three (WFC3) on Hubble has a larger field of view, significantly better detectors and superior sampling compared to camera 3 on NICMOS. The net improvement in survey speed is approximately a factor of 20. This enhanced survey speed does not fully capture the gains provided by WFC3. The quality of the spectra, in terms of resolution, a well-focused point spread function, and uniform sensitivity are also greatly superior to those offered by NICMOS.

In HST's Cycle 17, we began a new observing program of WFC3 pure parallels, the WFC3 Infrared Spectroscopic Parallel (WISP) survey. In ~ 250 orbits, the program will obtain near-infrared slitless spectroscopy of ~ 90 uncorrelated high latitude fields (PI=Malkan, GO-11696). This will produce a large sample of emission-line galaxies to measure the star formation rate continuously from at $z \sim 0.5$ to $z \sim 2.5$, over which ground-based searches are severely limited. The study of dust and metallicity in a large, unbiased sample of galaxies and the evolution of the star formation density are among the main goals of our project. In this paper, we present the analysis of the first 19 fields, from which we have selected high-confidence emission lines. In Sections 2 and 3, we describe the survey and data reduction. We discuss the results in Section 4, and finally offer some thoughts on the future possibilities in Section 5. Throughout, we assume a Λ -dominated flat universe, with $H_0 = 71$ km s^{-1} Mpc $^{-1}$, $\Omega_\Lambda = 0.73$, and $\Omega_m = 0.27$. All magnitudes are in AB system.

2. OBSERVATIONS

The infrared channel of the WFC3 utilizes a $1K \times 1K$ HgCdTe detector array. At a plate scale of 0.13 arcsec

px $^{-1}$, the total field of view covered is $123'' \times 136''$. There are two IR grisms on WFC3: G102 covering the $0.8 - 1.1$ μm range with a dispersion of 0.0024 $\mu\text{m}/\text{pixel}$ and G141 covering the $1.07 - 1.7$ μm range with a dispersion of 0.0046 $\mu\text{m}/\text{pixel}$. These correspond to average resolving powers for point sources of $R = 210$ for the G102 and $R = 130$ for the G141. For an unresolved line, the FWHM will be about 2 pixels. The details of the grisms and their characteristics can be found in Kimble et al. (2008) and on the WFC3 website⁹.

Each target field was observed briefly in direct imaging mode, using the broadband filter that matches the grism spectral coverage most closely: F110W for the G102, and F140W for the G141. As detailed in the next section, all of our observations were carried out in the ‘‘pure-parallel’’ mode with the Cosmic Origins Spectrograph (COS) or STIS operating as the prime instrument.

2.1. Pure Parallel Observation Scheduling

Pure-parallel observing with HST works as follows: Observing programs approved on COS and STIS constitute a parallel-observing ‘opportunity’ (see Table 1). Observations with these two instruments, by necessity, require stable, long integrations, which means that the entire focal plane of HST is held at a single pointing and fixed orientation angle for long periods of time. Thus it is simply a matter of turning on one of the other instruments in the focal plane to obtain quality data in a parallel field, offset by a $5.5'$ and $4.75'$ from the COS and STIS primary target, respectively. This motivated the strategy of a number of programs using WFC3 in parallel. Two other HST Cycle 17 programs were approved, both to do infrared direct imaging (GO-11702, PI = Yan; GO-11700 PI = Trenti). Pure-parallel observing is perfectly suited to the goals of the WISP Survey, since it allows us to obtain deep, continuous, IR spectroscopy in dozens of uncorrelated fields.

We selected our parallel targets with a preference for long integration times and high-galactic-latitude (> 30 degrees out of the galactic plane) fields. In order to reach similar depths in both the G102 and G141 spectra, we planned an $\sim 2.5:1$ G102:G141 integration time ratio. Additionally, the process of extracting the slitless spectra from the grism images requires direct imaging of the same fields (see Section 3) and so we obtained imaging in F110W and F140W (corresponding to J_110- and H_140-band, respectively) on the same orbits as the grism imaging with an $\sim 6:1$ grism:direct imaging integration time ratio. To date, we have received, reduced, and analyzed 19 fields (Table 1), the results of which are presented here.

Cycle 17 was the first year a powerful new procedure was adopted for scheduling and optimizing parallel observations. Unlike previous cycles, each of the Parallels teams was allowed to select individual observing opportunities, with accurately known durations of each orbital visit, well in advance. Since every parallel visit is unique, with its own combination of full- and partial orbits, we optimized each individual orbit to obtain the exposure time ratios mentioned above in the available time, thereby reaching a carefully balanced set of sensitivities. This tremendous improvement over earlier years

⁹ <http://www.stsci.edu/hst/wfc3/>

TABLE 1
SCHEDULE OF OBSERVATIONS TO DATE FOR THE WISP SURVEY

Field	Date	RA [HMS]	DEC [DMS]	Number of Orbits	F110W [Sec]	G102 [Sec]	F140W [Sec]	G141 [Sec]	Primary Proposal ID	Primary Visit No.	Primary Instrument
1	2009/11/24	01 06 35.29	+15 08 53.8	4	884	4815	506	2609	11720	01	COS
5	2009/12/20	14 27 06.64	+57 51 36.2	5	1034	5515	1034	5515	11720	13	COS
6	2009/12/24	01 50 17.18	+13 04 12.8	4	609	3609	862	5015	11727	09	COS
7	2009/12/25	14 27 05.91	+57 53 33.7	7	834	6318	1112	6224	11720	14	COS
9	2009/12/29	12 29 44.31	+07 48 23.5	4	759	4612	684	3712	11703	01	STIS
10	2010/01/02	09 25 07.84	+48 57 03.0	3	631	3909	406	2209	11742	06	COS
11	2010/01/03	11 02 17.38	+10 54 25.4	3	556	3709	456	2006	11742	07	COS
12	2010/01/04	12 09 25.25	+45 43 19.8	5	1312	8221	606	3009	11741	04	COS
13	2010/01/09	01 06 38.77	+15 08 26.2	3	556	3009	506	2409	11720	03	COS
14	2010/01/09	02 34 56.80	-04 06 54.5	4	834	6215	481	2809	11741	03	COS
15	2010/02/12	14 09 42.47	+26 21 56.0	5	1612	8321	531	2609	11741	26	COS
16	2010/02/16	02 34 54.72	-04 06 42.5	5	1087	6921	584	2509	11741	01	COS
17	2010/02/18	02 13 38.11	+12 54 59.3	3	534	3409	559	3409	11727	11	COS
18	2010/02/19	12 29 17.25	+10 44 00.6	5	534	3512	762	3824	11561	04	COS
19	2010/02/20	02 34 54.29	-04 06 30.5	5	1187	8721	484	2809	11741	02	COS
20	2010/02/21	14 09 41.15	+26 22 15.1	7	1815	8430	559	2812	11741	25	COS
21	2010/03/05	09 27 55.77	+60 27 05.3	1	0	0	353	2006	11728	10	COS
22	2010/03/05	08 52 44.99	+03 09 09.6	1	0	0	253	1806	11728	13	COS
23	2010/03/06	09 43 16.12	+05 27 37.1	3	0	0	681	4115	11598	42	COS

NOTE. — A summary of the observations performed under the HST program GO/PAR 11696 for the WISP Survey to date. Four additional fields were deferred to a later paper, because they require additional reductions. Note that some targets have more than 5 orbits of observations. These are not necessarily all full orbits, however, which is why, for example, a three-orbit observation may have more than half the total integration time of a six-orbit observation, and targets with the same number of orbits have varying total integration times.

of “generic” parallel visits has improved the efficiency of our observing program by about 50% for a fixed allocation of orbits. We also requested, and were granted, an additional 17 single-orbit parallel observations. Although these were too short for the purposes of other programs, when we observe these new parallel fields in only the F140W and G141, we are still able to reach comparable depths to the G141 images of many of our multi-orbit fields (See Table 1).

3. DATA REDUCTION

Slitless spectroscopy offers a considerable number of advantages for our WISP program. The high multiplexing capabilities offered by the WFC3 grisms combined with the observation of a significant number of uncorrelated fields offered by the pure parallel strategy, makes it perfectly suited for survey purposes. It allows a wide, uncontaminated spectral coverage with stable and accurate calibration. The ability to combine G102 and G141 grisms, with a well-behaved overlap gives the unique opportunity to find multiple lines per object at faint magnitudes. Because of the well-behaved photometry, it is possible to combine the spectra with broad-band photometry to provide comprehensive and precise spectral energy distribution (SED). Moreover, the use of the HST offers a much lower sky background level compared to the ground. However, to fully exploit the potential of this tool, one needs to overcome some limitations. In crowded fields, object spectra and orders sometimes overlap, leading to confusion in the spectral extraction and to uncertainties in the background estimate. Given the high latitude of the WISP fields, crowding did not represent a problem in our observations. The spectral resolution is determined by the size of the target: for point-like sources, this corresponds to the instrument Point Spread Function (PSF), while for extended sources it is the spatial extent of the object in the dispersion direction.

This basic principle of the slitless reduction is the use of the direct images to provide the input catalog of objects. The object positions, sizes and shapes are then used - in conjunction with a precise knowledge of the mapping between the direct and the dispersed frames to extract photometric and wavelength calibrated 2D and 1D spectra from the data using a 3D flat-field cube which contains the calibration of each detector pixel for each wavelength. This process has been integrated with the WFC3 pipeline (CALWF3 version 2.0) with the provision of the aXe software (Kuemmel et al. 2009a) which has been developed to handle all of the HST slitless spectroscopic modes. aXe maps not only the + first order spectra but also the zeroth, - first, +/- second and higher order spectra which allows the quantitative estimation of contamination in the case of overlapping objects.

We processed all the data (including both grism and direct imaging exposures) using the CALWF3 pipeline (version 2.0). Direct images were corrected for bias, dark, flat-field and gain variation using the best reference files obtained from the STScI archive. WFC3 performs multiple non-destructive reads in the slitless spectra in MULTIACCUM mode with the sampling sequence SPARS100. This allows cosmic ray rejection in a single exposure sequence. The reduction pipeline fits the accumulating signal in the the MultiAccum readouts to identify the cosmic rays. In the slitless grism data, pixels cannot be associated with a unique wavelength. For this reason, CALWF3 applies a unity flat so that no pixel-to-pixel correction is applied at this stage. The proper flat-fielding is then applied during the extraction of the spectra with aXe.

3.1. Direct Images

Because our pure-parallel observations do not allow dithering, the processed images still contain a significant number of bad pixels that were not identified during the

CALWF3 step. In addition, CALWF3 fails to properly flag a fraction of cosmic ray hits, when these were impacting multiple pixels. We identify and flag these pixels in the data quality (DQ) masks using custom IDL routines. Finally, the images are combined with the IRAF task MULTIDRIZZLE (Koekemoer et al. 2002) using standard parameters. This step also corrects for bad pixels and cosmic rays, and removes the geometric distortion using the latest distortion solution (IDCTAB) files. The final drizzled images have accurate astrometry and a uniform photometry across the image.

The position of the spectra in the dispersed images is determined by the location of the objects in the corresponding direct exposure. We run SExtractor (Bertin & Arnouts 1996) on the drizzled direct images, creating independent source catalogs for the F110W and F140W images. For the source detection we used the RMS weight maps derived during the MULTIDRIZZLE step. Every source in the catalogue is required to have at least 6 connected pixels (DETECT_MINAREA = 6), with values above 3.5σ (DETECT_THRESH = 3.5σ). Finally, the catalogs generated for the F110W and F140W images are matched and put on the same numbering scheme. The individual detection in both filters allow us to keep objects detected in only one band and ensures an accurate astrometry between the grism image and the reference direct one. Because aXe performs the spectral extraction on individual (not distortion-corrected) grism frames, the combined catalog is projected back to these frames to generate an input object list (IOL) of coordinates for each grism frame to be used in the aXe extraction. Starting from these IOLs, the aXe software computes the reference position and spectral trace for each object in the dispersed images.

3.2. Grism Images

Before proceeding to the actual spectral extraction, the sky background must be estimated and subtracted from each grism frame. It is possible, within aXe, to estimate the background locally by interpolating on the sky regions above and below the spectral trace. However, we decided to perform a global sky subtraction on the entire image before proceeding to the extraction of the spectra. This method proves more efficient for slitless survey data (Pirzkal et al. 2004), where spectra may be contaminated by the trace of nearby objects, and multiple orders.

In the slitless mode, each spatial element of the detector receives the full sky and telescope foreground emission integrated over the grism bandpass. The grisms disperse the foreground light, but the lack of a slit results in a mapping of spatial to spectral domains that reintegrates uniform sources (e.g., the sky) effectively into undispersed emission. A portion of the detector does not receive the full zero-order sky and thus there is a ramp in the sky in the first one hundred or so columns on the detector. The sky foreground in the G141 and G102 grisms is a combination of zodiacal light, earth limb and thermal emission from the telescope. The processed two-dimensional grism images contain a significant signal from these sources that must be removed for proper photometric calibration, as well as for optimal identification of spectral features.

We constructed a master sky template for each grism by making a stack of all of our grism exposures. The in-

dividual images were first scaled using the image mode, then combined with a median stack. The resulting master sky contains low-level residuals from bright sources, but these have little impact on our results. Our sky template is being improved as additional independent fields are observed and added to the master sky.

For each grism observation we scaled the appropriate master sky and subtracted this from the post-pipeline two-dimensional image. We experimented with scaling the sky by the mode of the pixel distributions and by minimizing the sigma in the sky subtracted image. These two approaches gave nearly identical results, and we proceeded with the skies scaled using the mode. The scale factors varied by more than a factor of two from one field to another, reflecting the changing zodiacal light background and contribution from the Earth's limb.

As in the direct images, the CALWF3 processed data still showed residual bad pixels and cosmic rays. We constructed a bad-pixel mask in which we flagged all bad pixels, including those with low-QE and with high value of the dark current. We then interpolated over these flagged pixels along the dispersion direction using a second order polynomial. We find that the majority of the bad pixels are isolated, and most interpolations were over at most 3 pixels. Thus the interpolation step does not introduce spurious features into the spectra. Moreover, because the position of each bad pixel is recorded in the masks, we have checked that the identified emission lines (see below) were not impacted by the interpolation process. Finally, we created the final dispersed images by averaging together the corrected frames, weighting each image by its exposure time. These frames were used in our visual inspection.

We also run MULTIDRIZZLE on the individual grism frames. This has the advantage of performing cosmic ray rejection and flagging the affected pixels in these frames. However the drizzled grism image is not used for extraction. The aXe procedure extracts the spectra from the individual grism images and all flagged pixels will be ignored during this process. Another advantage of applying MULTIDRIZZLE on both direct and grism frames is to avoid potential differences in the WCS data for the two images that could lead to a mismatch in the source positions in the direct and grism individual images during the extraction.

3.3. aXe Extraction

The spectral extraction is performed with the slitless extraction package aXe (version 2.0) developed at Space Telescope European Coordinating Facility (ST-ECF). The input image list is prepared with each individual grism image paired with the direct image which is closest in time and its SExtractor catalog. We used the latest in-orbit configuration files (Kuntschner et al. 2009a,b) and thermal vacuum (TV) 3 sensitivity calibrations. Some of these reference files will be improved for later reductions. We compared several apertures and orientation parameter setups to optimize the extraction. We used an aperture width of twice the object size listed in the input object list, and an extraction direction perpendicular to the spectral trace (see aXe user manual¹⁰ for details).

¹⁰ http://www.stecf.org/software/slitless_software/axe/

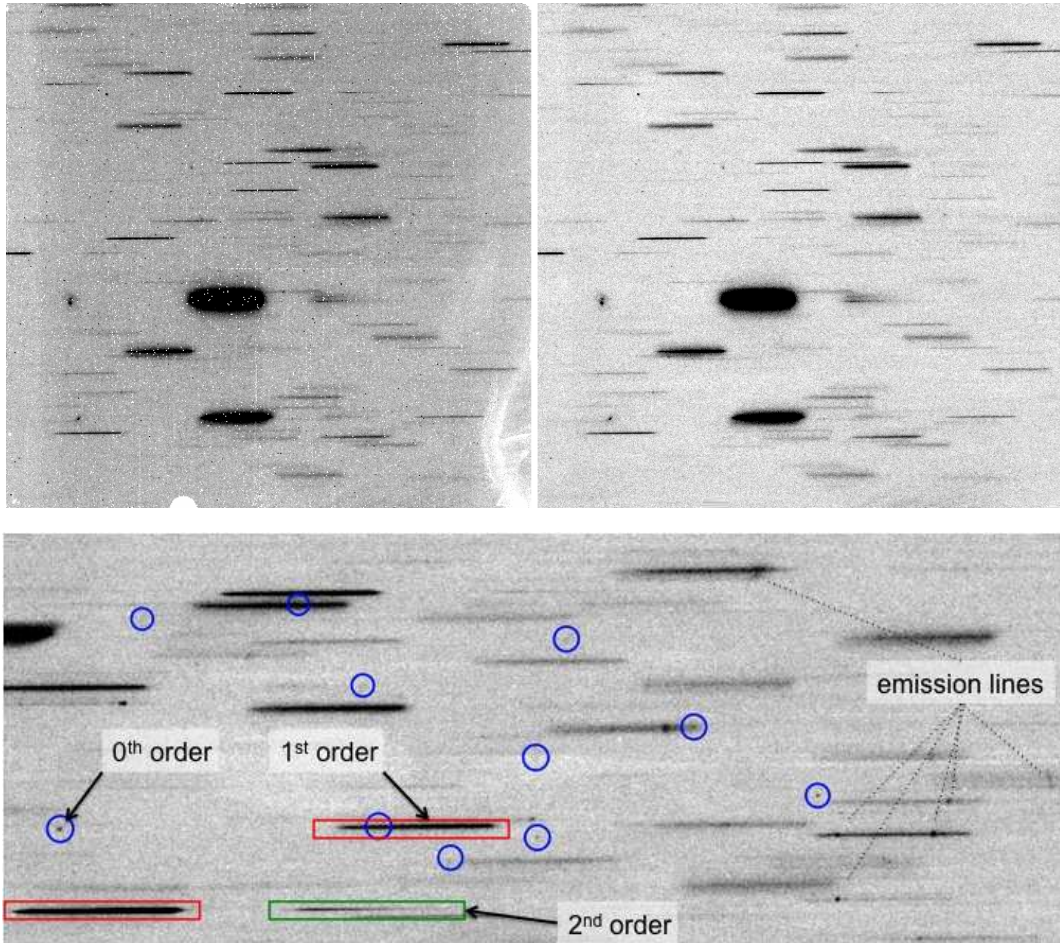


FIG. 1.— *Top panel* shows a comparison of an individual G141 grism image before and after the reduction process. The raw image on the left shows a large number of bad pixels and cosmetic artifacts that are no longer visible on the clean image. *Bottom panel*: An example of different spectral features in our grism images. Red and green rectangles indicate examples of first and second order spectra respectively. The blue circles mark the zero order positions, indicating in some cases a contamination to the spectra. Some emission lines are also indicated.

Two-dimensional cutout spectra of each object in each exposure are extracted and then combined (with aXeDRIZZLE) to create a final high signal-to-noise (S/N) ratio spectrum. The combined 2D spectrum is then used to extract the final object spectrum. We used optimal extraction to increase the S/N ratio of the extracted spectra. The spectral contamination by spectra of nearby objects is estimated by aXe using the object positions and magnitudes in the direct image. We adopted the Gaussian emission model, using SExtractor size parameters, to approximate the object morphology. The simulated spectrum is then extracted and used to estimate the contamination to each object.

3.4. Emission line Objects

Each stacked two-dimensional grism frame was searched visually by two or more of the authors. We used the dispersion solution from the WFC3 configuration files to determine the positions of the aperture beams in both grisms. The 1st order of each object is then marked with the corresponding aperture beam and the original ID number in the IOL. The actual search area is about 3.3 arcmin^2 , smaller than the IR channel field of view. Because of the shift between direct and grism images, spectra on the left part of the field do not have detections in the direct image, and zeroth orders cannot be

identified at the far-right side of the frame. Some examples of 1st and 2nd order aperture beams are shown in Figure 1 by the long rectangular boxes.

Besides the overlap between the objects, the most important spurious feature is the zero-order image. Because the light is not dispersed, the zero-order image could be easily confused with an emission line. We derived the position of all the zero-orders in the grism exposures, using the positions of all the sources in the direct images. We marked the zero-orders in the grism exposures to be able to exclude them during the visual inspection of the grism images. In Figure 1 we show an example of this procedure: the blue circles show the zero order location of some of the objects detected in the direct images. With all possible contaminants identified in the grism images, we proceeded to compile a list of all emission-line source in each field. We compared the G102 and G141 spectra of each field side-by-side, to aid in the identification of genuine emission-lines. In many cases the identification of the lines is unambiguous. For example, galaxies with $H\alpha$ often also have detectable [SII]6717/6731 and sometimes [SIII]9069,9532 emission (Figure 2). Strong [OIII]5007,4959 emission in the G102 grism is easily recognized on the basis of $H\alpha$ in the G141 and often $H\beta$ in the G102 spectra, even though the two [OIII] lines are blended (see Figure 3). At higher redshifts, strong

[OIII]5007,4959 in the G141 grism is confirmed by faint $H\beta$ emission. In some cases [OII]3727 can be seen in the G102 spectra for sources with strong [OIII]5007 in the G141 spectra (Figure 4).

There are a large number of objects with only a single faint emission-line in the full spectral range covered by the two grisms. It is most probable that these are weak $H\alpha$ emission lines for which we are unable to detect other lines. However, since we see many [OIII]/ $H\alpha$ pairs up to $z \sim 1.5$ we expect, in absence of other indication, to have a fraction of the single lines in the G141 that would correspond to [OIII] whereas $H\alpha$ has moved out of the G141 grism. The [OII]3727 line is seldom recognized as a redshift indicator by itself, since in this case it is more likely to be an $H\alpha$ line at low- z rather than a high- z [O II] line. There are some objects, however, for which we believe the single line in the G141 spectrum is [OIII]5007,4959. This is primarily based on the lack of continuum in the G102 spectra, indicative of the fall off in the continuum below the Balmer and 4000 angstrom breaks.

Each emission feature was assigned a confidence flag, ranging from 0 to 4 in order of decreasing confidence. The highest confidence level (class 0) was assigned to objects with multiple emission features and unambiguous redshifts. Confidence classes 1, 2 and 3 were assigned to single features with unambiguous identifications (class 1), good quality (class 2), moderate quality (class 3), and uncertain (class 4, which are not included in the present analysis). Similar confidence classes have been used in ground-based redshift surveys (e.g. CFRS, Le Fevre et al. (2005); GDDS, Abraham et al. (2004)) and have been found to be useful in restricting various types of analysis to high confidence objects. Monte Carlo simulations will be used to assess the flux completeness and reassess the confidence levels when the data set is complete.

The final object catalog contains a measurement of each emission line, performed using a custom IDL fitting tool, and relevant information from the object extraction. The line fitting uses the pixel position of the identified lines, applies the grism dispersion solution to find the corresponding wavelength and therefore the redshift of the object. The fitting model consists of a polynomial continuum and a gaussian (a multi-gaussian model is used to deblend the $H\alpha$ -[SII] and [OII] λ 5007,4959 Å lines). The program fits the identified lines by least squares, and tries to fit potential lines that could be present in the spectrum at the correct redshift with a lower significance of typically 2σ . The entire process is visually monitored by displaying the line, the fit model and the robustness of the fit. The fitting flux uncertainties are derived from our aXe extraction and calibration. As an independent check, a large subset of these same emission lines were also measured by hand, using the SPLOT task in IRAF. The resulting plot measurements generally agree with the automated measures to within the uncertainties.

We investigated the accuracy of the grism data calibration. First, we compared the fluxes of lines detected simultaneously in both G102 and G141 grisms, in a wavelength domain restricted to a throughput higher than 10%. In most cases the flux agrees to better than 10% between the two grisms. Second, we compared the agreement between wavelength calibrations by using the over-

lapping region around 1.15 micron, and the redshift determined independently from different lines detected in G102 and G141. We observed a typical offset of 2×10^{-3} microns that is within the uncertainties of the redshift determination in the individual grisms.

3.5. Grism Sensitivities

Due to the pure parallel nature of our program, we have no control over the location and timing of our observations. Because of this, we are subject to a variety of visit durations (typically 3-5 orbits), number of readouts, and backgrounds (zodiacal light and earthshine), all of which affect the sensitivity of our observations. In order to determine the depth of our spectroscopy, we have measured the background rms (in electrons per second) of every final reduced grism image. This rms is then divided by the sensitivity (as a function of wavelength) and divided again by the dispersion (in Å pixel⁻¹) to give the 1σ noise as a function of wavelength. In Figure 5 we plot the 5σ continuum sensitivity in a five-pixel wide aperture (in the spatial direction) for each pointing. We used three pixels width in the dispersion axis to estimate the line sensitivities. Each field has been scaled by (exptime)^{1/2} so that the relative depths are comparable. Though most observations agree with the predicted depths from the WFC3 exposure time calculator, there is a large dispersion in the depths due to background variations, and any given field can vary substantially from the mean by typically 20% (up to $\sim 50\%$). We also plot in Figure 6 our line sensitivity as a function of depth. In both grisms, we reach a median depth of about $\sim 5 \times 10^{-17}$ ergs s⁻¹ cm⁻².

In summary, for the typical exposure times of the survey (~ 6400 s in G102, ~ 2700 s in G141) we are able to detect (at 5σ) compact lines with $f = 5 \times 10^{-17}$ ergs s⁻¹ cm⁻² at $0.95 < \lambda < 1.17$ Å and $1.3 < \lambda < 1.65$ Å.

4. EMISSION LINE RESULTS

To date, we have selected emission lines over 19 WFC3 fields, and measured redshifts and line fluxes from the highest confidence emitters. While incomplete at the faintest lines, we clearly reach emission line fluxes down to a few $\times 10^{-17}$ erg s⁻¹ cm⁻², often in the presence of a second brighter line. At the highest confidence levels, our preliminary analysis yields 328 (S/N > 5) emission lines from 229 objects in our 19 WFC3 fields. Simulations will be required to determine our incompleteness due to extended emission, confusion, both high and low equivalent widths, while accounting for the non-uniform survey sensitivity shown in Figure 5. We list the identifications of these lines in Table 2. We note that the fraction of sources with multiple emission lines increases if we include lines detected at 3σ to 5σ .

We find 185 galaxies with likely or definite $H\alpha$ emission. Amongst these, 56 have secure identifications based on multiple emission lines. We also identify single-line objects as $H\alpha$ emitters, as was the case with NICMOS grism spectroscopy (McCarthy et al. 1999; Hicks et al. 2002; Shim et al. 2009). This assumption has generally worked in ground-based narrow-band IR detections of single emission lines (e.g. Bunker et al. 1995; Malkan Teplitz & McLean 1996; van der Werf et al. 2000; Sobral et al. 2009).

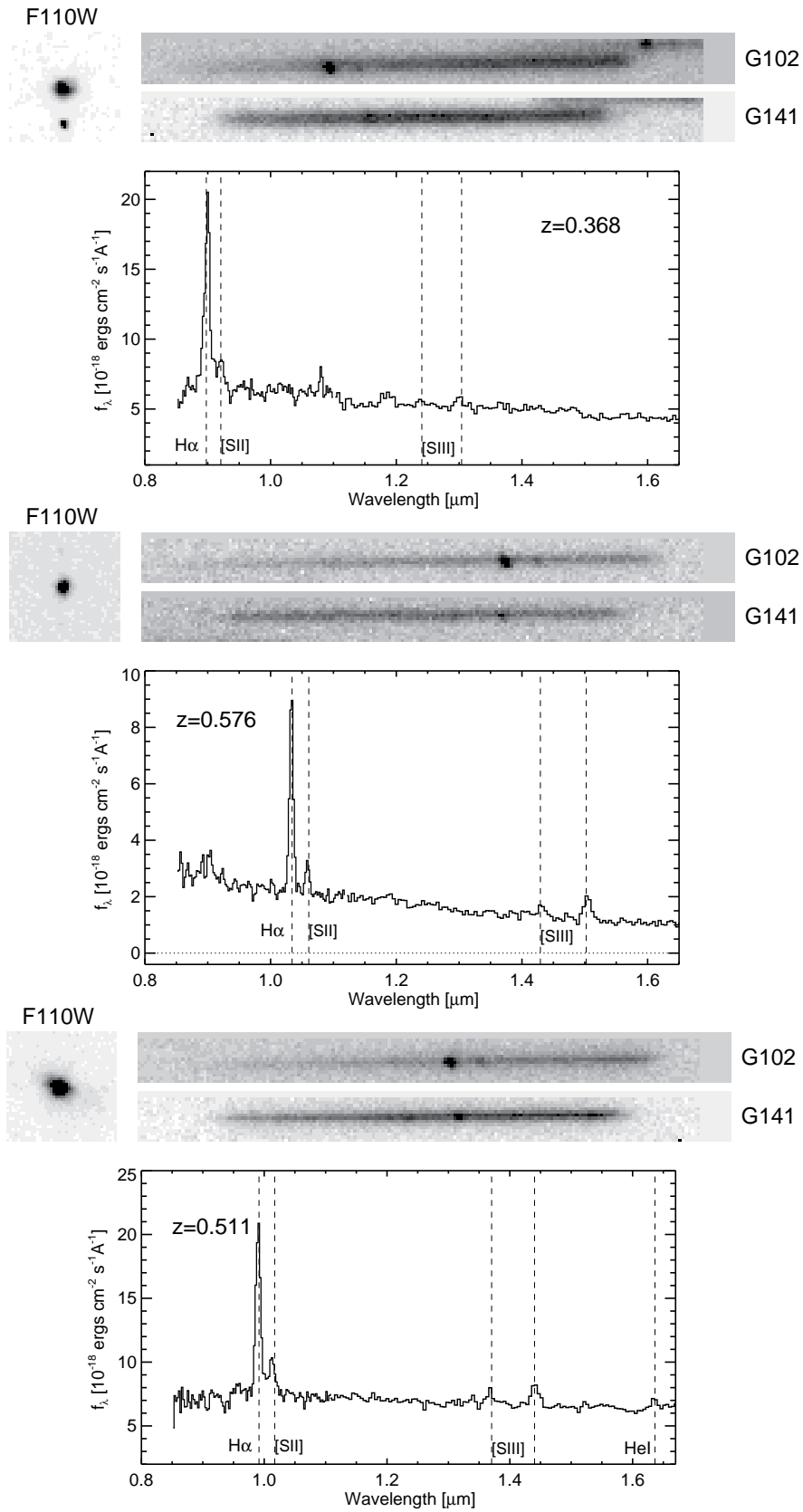


FIG. 2.— Examples I: low-redshift emission line objects at $0.4 < z < 0.8$. For each object we show the direct image cut-out ($5'' \times 5''$), the 2D G102 and G141 grism spectra and the 1D extracted spectrum at observed wavelength. In this category, H α falls in the G102 grism. We can see several emission lines: [S II] $\lambda\lambda 6716+6732$ \AA , [S III] $\lambda 9069$ \AA , [S III] $\lambda 9532$ \AA and He I $\lambda 10830$ \AA .

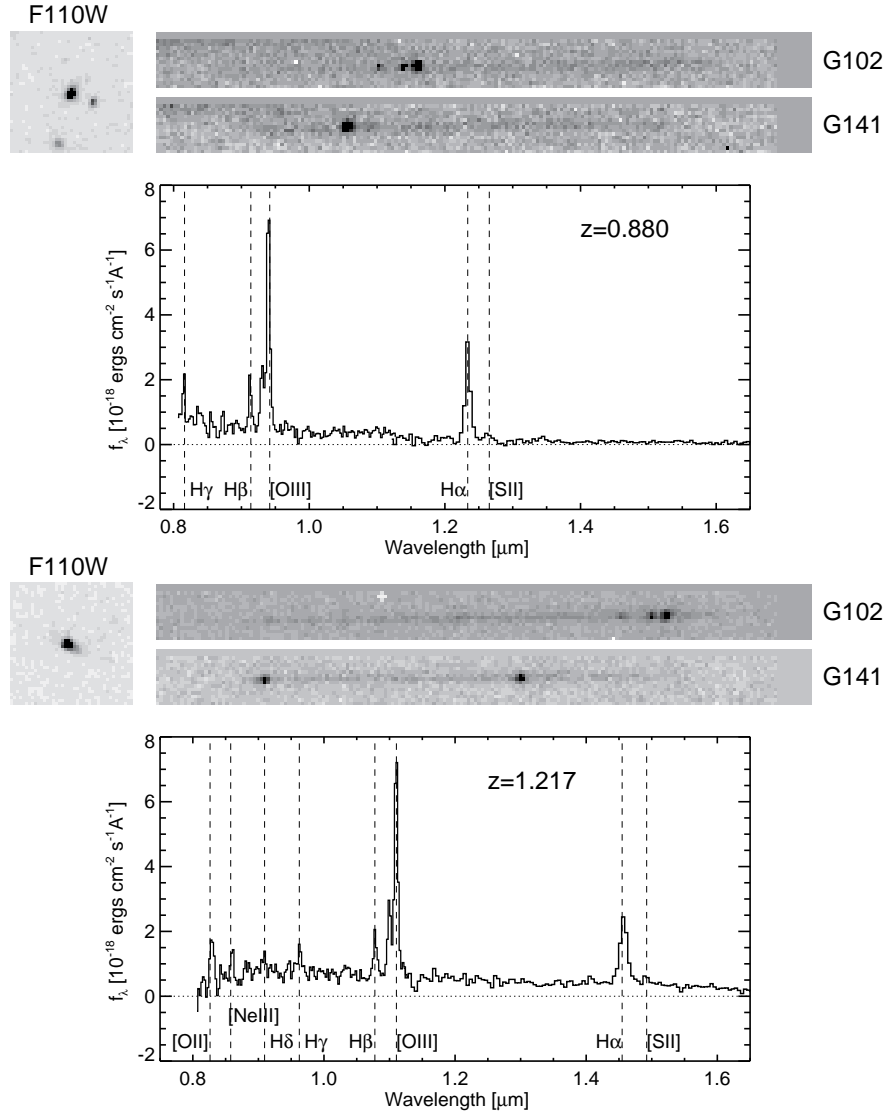


FIG. 3.— Examples II: emission line objects in the redshift range $0.6 < z < 1.3$. For each object we show the direct image cut-out ($5'' \times 5''$), the 2D G102 and G141 grism spectra and the 1D extracted spectrum at observed wavelength. This category includes mainly $\text{H}\alpha$ [O III] line emitters, but we also observe [O II], [Ne III], $\text{H}\beta$, $\text{H}\gamma$ and $[\text{S II}]\lambda\lambda 6716+6732 \text{ \AA}$.

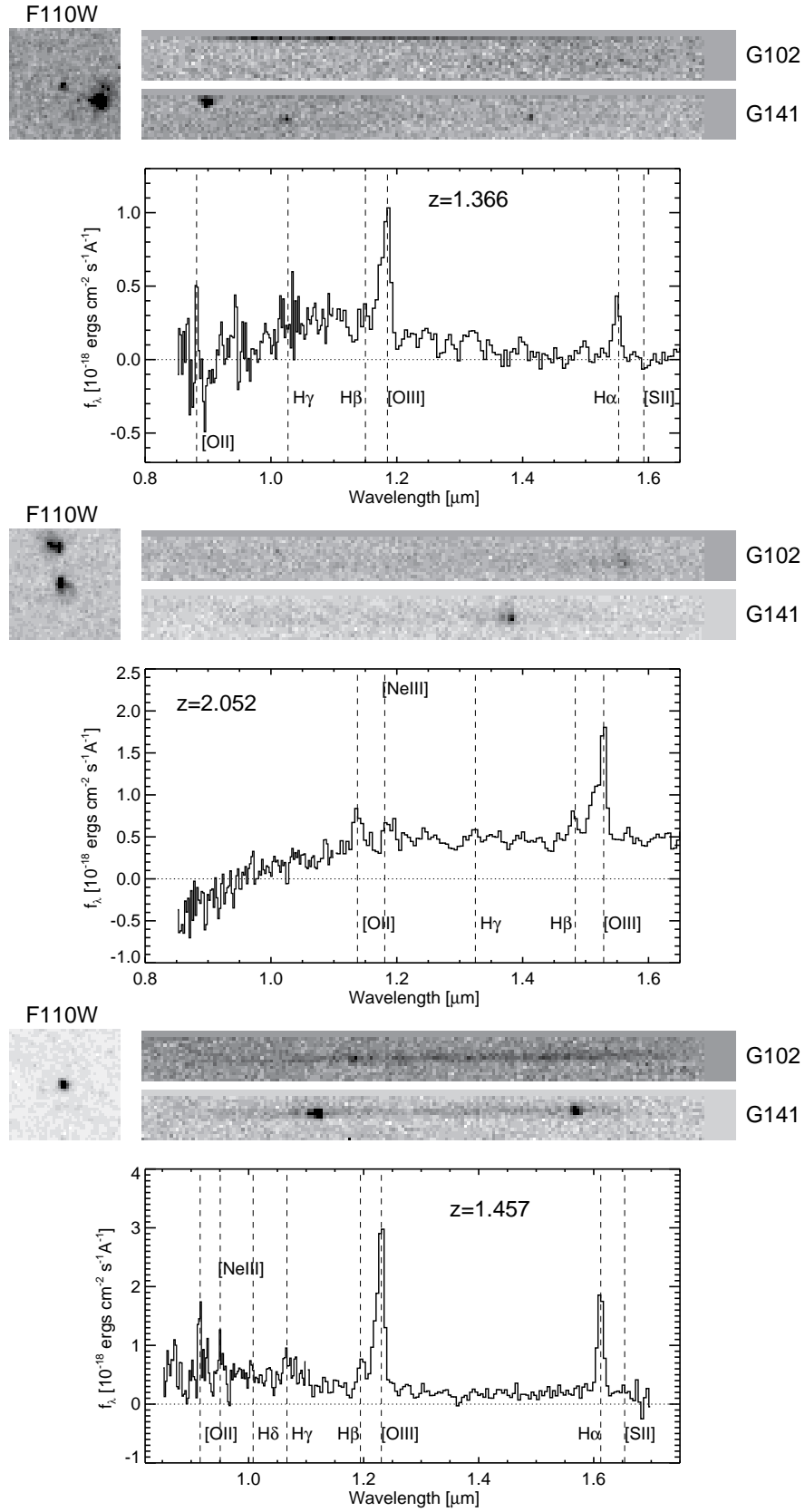


FIG. 4.— Examples III: high-redshift emission line objects between $1.3 < z < 2.3$. For each object we show the direct image cut-out ($5'' \times 5''$), the 2D G102 and G141 grism spectra and the 1D extracted spectrum at observed wavelength. At these redshifts, both $H\alpha$ and [O III] are shifted to the G141 grism. In many cases we also observe the [O II] emission line in the G102 grism.

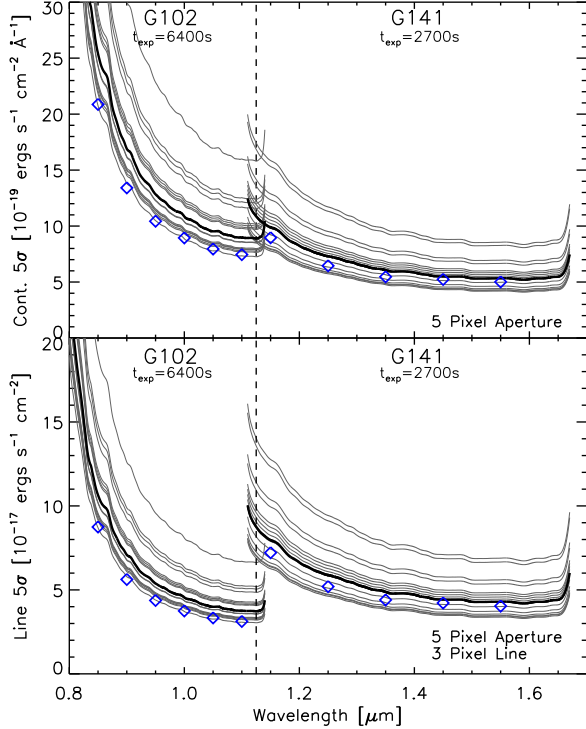


FIG. 5.— The 5σ continuum (top) and line (bottom) sensitivities as a function of wavelength. The depth of each field is plotted in gray and scaled (by $\text{exptime}^{1/2}$) to the “nominal” survey exposure times. The thick solid lines denote the median field depth. The blue diamonds are the values given by the exposure time calculator assuming “average” earthshine and zodiacal light backgrounds. A five-pixel ($0.65''$) wide aperture was used for these estimates and the line sensitivities assumed three pixel widths in the dispersion direction. More compact sources will give slightly better sensitivities. There is significant scatter from the median due to variations in background levels.

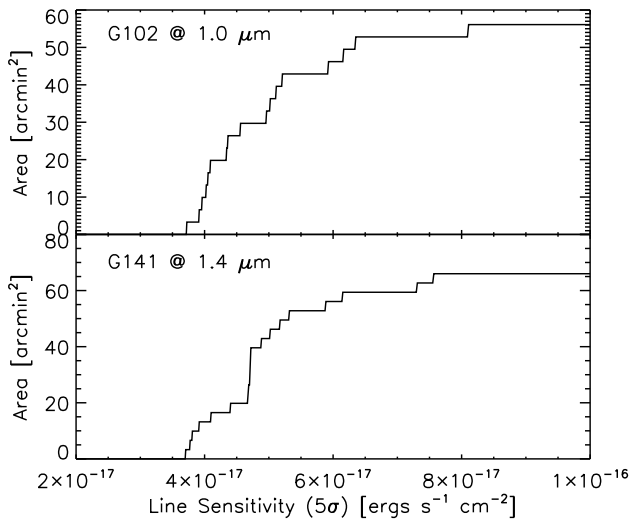


FIG. 6.— Cumulative area as a function of depth. Each field has an effective area of 3.3 arcmin^2 which is added to the cumulative area at the value of its five sigma line sensitivity (in a 5×3 pixel region). The depth varies as a function of wavelength so we choose to use the depths at the central wavelengths ($1.0 \mu\text{m}$ for G102 and $1.4 \mu\text{m}$ for G141). The depths are better at longer wavelengths and worse at lower wavelengths. The median depths in both grisms are $\sim 5 \times 10^{-17} \text{ ergs s}^{-1} \text{ cm}^{-2}$.

TABLE 2
EMISSION LINES IN THE WISP SURVEY

Line	Number Detected
Single lines	129
H α confirmed	56
H β	5
[OIII] 5007	59
[OIII] 4959	35
[OII] 3727	15
[SII] 6717 + 6731	15
[SII] 9069	3
[SII] 9532	5

NOTE. — The main emission lines with a signal to noise ratio $S/N \geq 5$ detected in the WISP Survey.

Other possible line identifications would almost always result in a brighter line that we would also detect. The most significant possibility of a single emission line that is not H α , would be [OIII] 5007+4959. This does occasionally happen in ground-based near-IR searches (Teplitz et al., 1999). Not surprisingly, for the remaining 56 objects with multiple bright emission lines, the most common combination is H α + [OIII] 4959/5007. The redshift distributions for the total sample is shown in the left panel of Figure 7, while the right-hand panel shows the redshift distribution for the H α , [OIII], and [OII] emitters separately.

We next compare these first results to our previous NICMOS H α survey (McCarthy et al. 1999; Shim et al. 2009). With WFC3, we see H α emission from $0.3 < z < 1.5$, whereas with the NICMOS G141 survey we were sensitive to H α from $0.7 < z < 1.9$. In the left panel of Figure 10, we plot raw number counts for the H α and single line emitters separately (red and blue points respectively) then for the total (H α + single-line) sample (black). We then compare total counts from both surveys, in the overlapping redshift range of $0.7 < z < 1.5$ (right panel). At the brighter end, we find a good agreement between the WISP survey and the NICMOS grism results, even without including the many lines which we have identified with a lower signal-to-noise ratio. But WFC3 starts to detect more galaxies than NICMOS at $f \sim 3 \times 10^{-16} \text{ ergs s}^{-1} \text{ cm}^{-2}$. Towards the faint-end and the completeness limit of NICMOS, the surface density of H α emitters detected with WFC3 is a factor of 3 higher. This is because our survey is more complete for extended line-emission and our spectra are sensitive to a very wide range of emission line equivalent widths, from cases where the continuum is hardly detected ($\text{EW}_{\text{obs}} > 300 \text{ \AA}$, see Figure 9), to low contrast features with EW as low as 15 \AA for lines that satisfy $S/N = 5\sigma$.

As Figure 8 illustrates, we routinely detect emission-lines in galaxies with luminosities well below L^* . Many of these very faint galaxies have strong [OIII]5007 emission and relatively weak [OII] and H β emission, suggestive of low metal abundances. The near-IR photometry provided by our F110W and F140W images, and ground-based follow-up (where practical), will allow us to extend pioneering work on the mass-metallicity relation at $0.5 < z < 1$ (Savaglio et al. 2005) and $1 < z < 3$ (Erb et al. 2006) to significantly lower stellar masses. The mass-metallicity relation is a critical diagnostic of

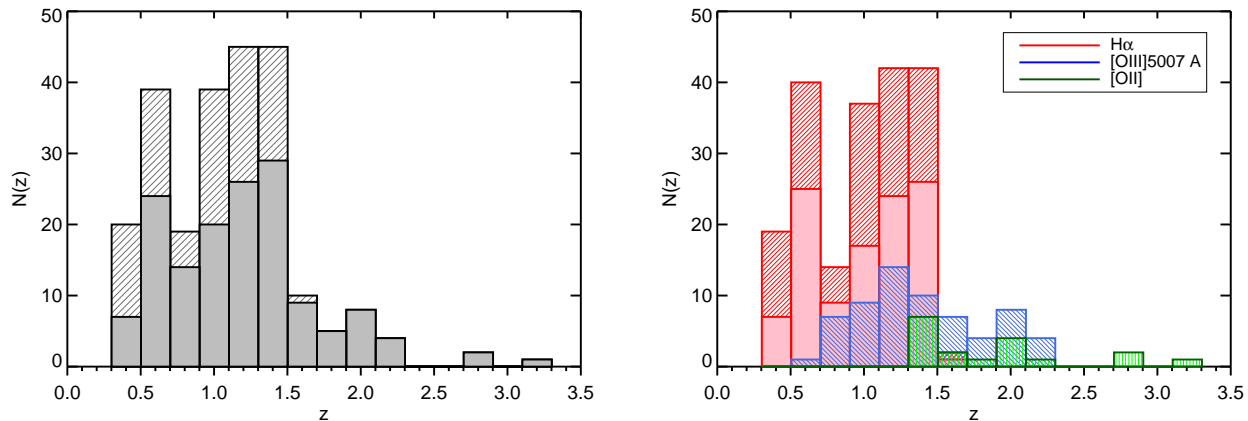


FIG. 7.— *Left*— The redshift distribution of our total sample of emission-line galaxies in 63 arcmin² of the WISP survey. Filled histogram represents our secure redshift determination (class 0 and 1), whereas on the top, the hatched part shows the uncertain single-emission-line objects assumed to be H α emitters. *Right*— The redshift distribution of our galaxies according to their emission lines. Again the hatched part of the H α emitters represent uncertain redshifts.

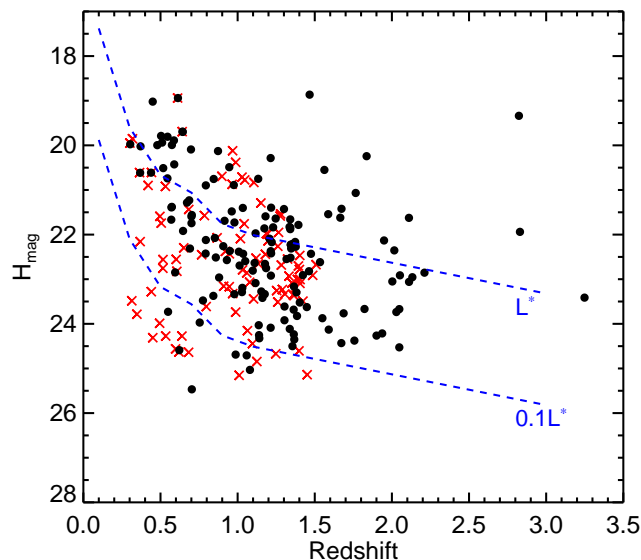


FIG. 8.— H₁₄₀-band magnitude as a function of redshift. Secure redshifts are shown as black circles and single line (assumed to be H α) emitters as red crosses. We also show the apparent H₁₄₀-band magnitude for L^{*} (and 0.1 L^{*}) galaxies derived from rest-frame near-IR (at low- z) and optical (at $z > 0.7$) luminosity functions (Bell et al. 2003, Faber et al. 2007, Shapley et al. 2001).

galaxy formation and evolution models as it is sensitive to a number of physical process (e.g. infall, SNe feedback, IMF).

In Figure 11 we plot on the left panel the observed star formation rate distribution of our H α sample derived from the H α luminosity using the Kennicutt (1998) conversion. Following Shapley et al. (2005), we corrected the H α fluxes for 20% average [NII]6584+6548 contribution, but no extinction correction is applied. On the right panel we plot SFR(H α) versus rest-frame R-band luminosity. For rest wavelength R magnitudes we used the F110W photometry if the observed wavelength of H α is $< 1.25 \mu\text{m}$ ($z < 0.9$) and the F140W photometry for H α $> 1.25 \mu\text{m}$ ($z > 0.9$), applying only the $(1+z)$ correction (without any k-correction). There is no extinction correction for the R-band magnitudes. The median SFR is 4 M $_{\odot}$ /year, and the median M_R of line-detected galax-

ies is -20.75, one and half magnitudes below L^{*} for $z \sim 1.0$ (Chen et al. 2003; Colbert et al. 2006). At the lower redshifts, especially for compact objects, our survey is able to detect lines in extraordinarily faint galaxies (M_R > -19), and star formation rates less than 1 solar-masse per year.

4.1. Absorption Line Spectra

Although we have so far limited the analysis to emission lines, the broad wavelength coverage and high sensitivity of the WISP survey leads also to a wealth of information from continuum spectra. The 4000Å break and the convergence of the Balmer series at 3650Å, provide two of the best low-resolution diagnostics for redshift and stellar populations. Continuum spectral diagnostics, particularly at $z > 1$, provide constraints on the mean age of the stellar population and the time since the last major episode of star formation. Spectroscopy of red galaxies from the ground in the visible is limited to objects with $z < 1.8$ and $I < 25$ (e.g. McCarthy et al. 2004; Cimatti et al. 2004; Doherty et al. 2005). Near-IR spectroscopy can probe to higher redshifts, but this is quite challenging (e.g. Kriek et al. 2008) and has been limited to small samples to date (e.g. Doherty et al. 2006). The WFC3 grisms are providing low-resolution continuum spectroscopy of red galaxies in large numbers with great sensitivity (e.g. van Dokkum & Brammer 2010). In Figure 12 we show an example of a post-starburst galaxy at redshift $z = 1.68$. A clear Balmer break is seen in the G102 spectrum, as well as absorption lines in the G141 part. A stellar population model is overplotted, giving an age of 600 Myr and an extinction of $A_V = 1.2$. This object has been pre-identified searching for galaxies with $H_{140AB} < 22$ and $J_{110} - H_{140} > 0.6$. This selection isolates bright passive galaxies at $z > 1$.

5. DISCUSSION AND SUMMARY

We have presented the first analysis of the WISP Survey of slitless spectroscopy with the NIR channel of WFC3, taken in pure parallel mode. In the first 19 fields, we surveyed 63 arcmin². At the highest confidence level we have detected 229 emission line objects. We reach typical 5σ sensitivities of $f \sim 5 \times 10^{-17}$ ergs s⁻¹ cm⁻² for compact lines.

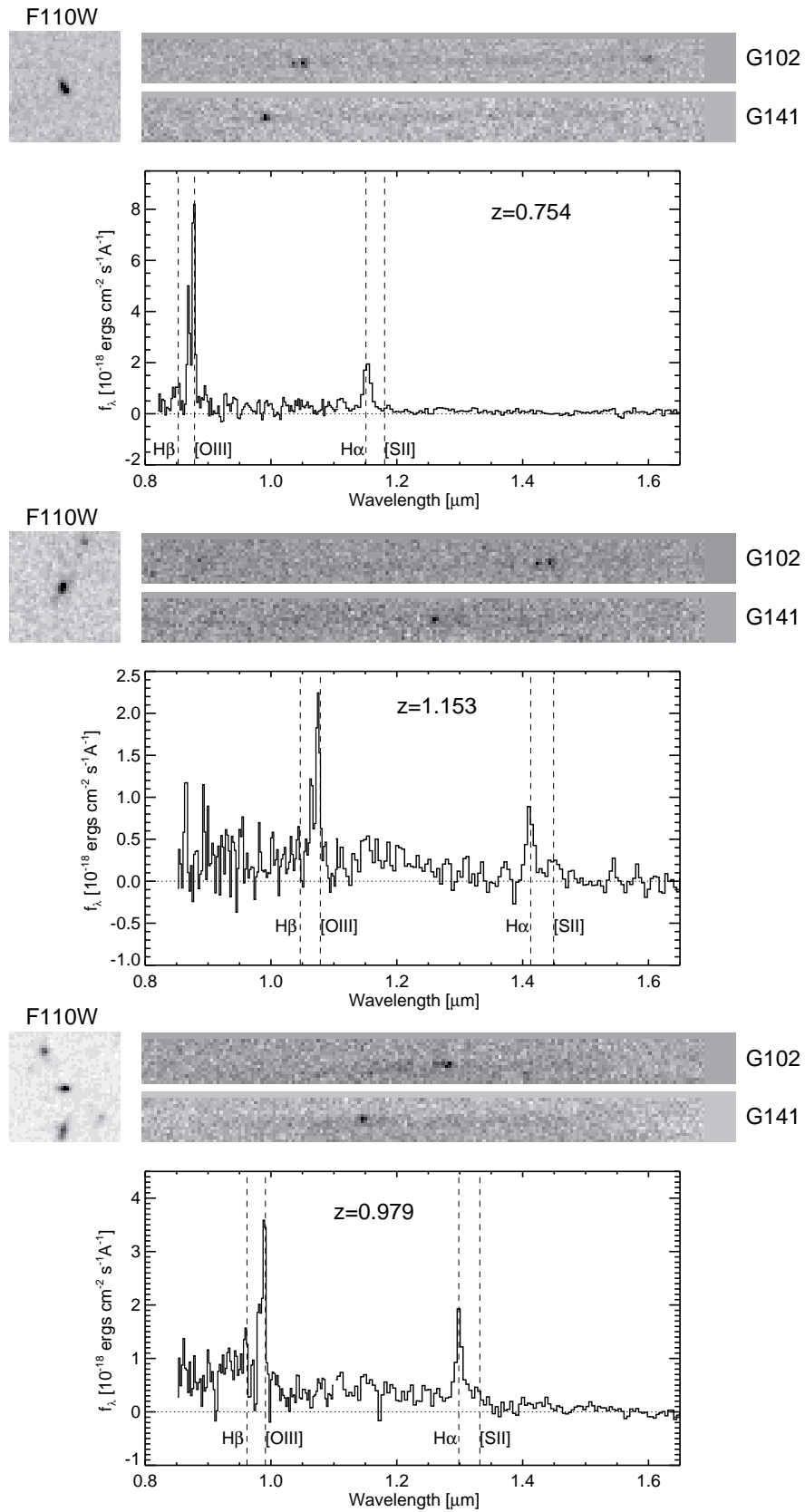


FIG. 9.— Examples IV: very high equivalent width emission line objects. A strong emission line is observed in this group of galaxies with an extremely faint continuum which barely visible in the 2D grism images. For each object we show the direct image cut-out ($5'' \times 5''$), the 2D G102 and G141 grism spectra and the 1D extracted spectrum at observed wavelength.

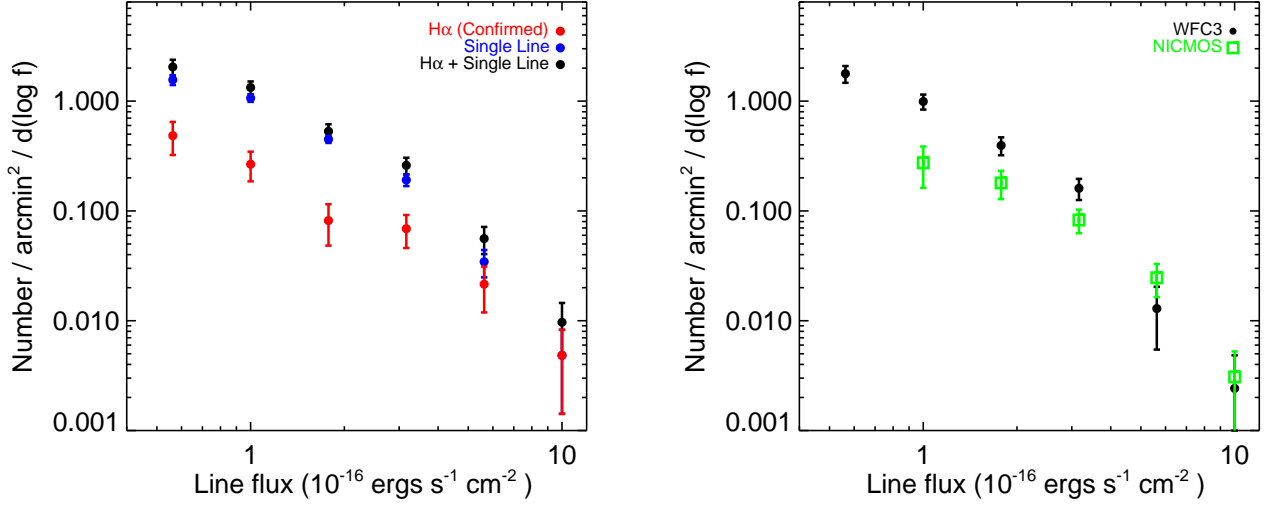


FIG. 10.— *Left*—Number counts of $H\alpha$ emitters in the WISP survey. Confirmed $H\alpha$ emitters are shown in red points, single-line emitters in blue and the total counts in black. *Right*— Number counts of $H\alpha$ and single line emitters in the WISP survey (black points) compared to the NICMOS Parallel grism survey (green squares), tabulated in the overlapping redshift range of $0.7 < z < 1.5$. Counts are given per $d(\log f) = 0.25$.

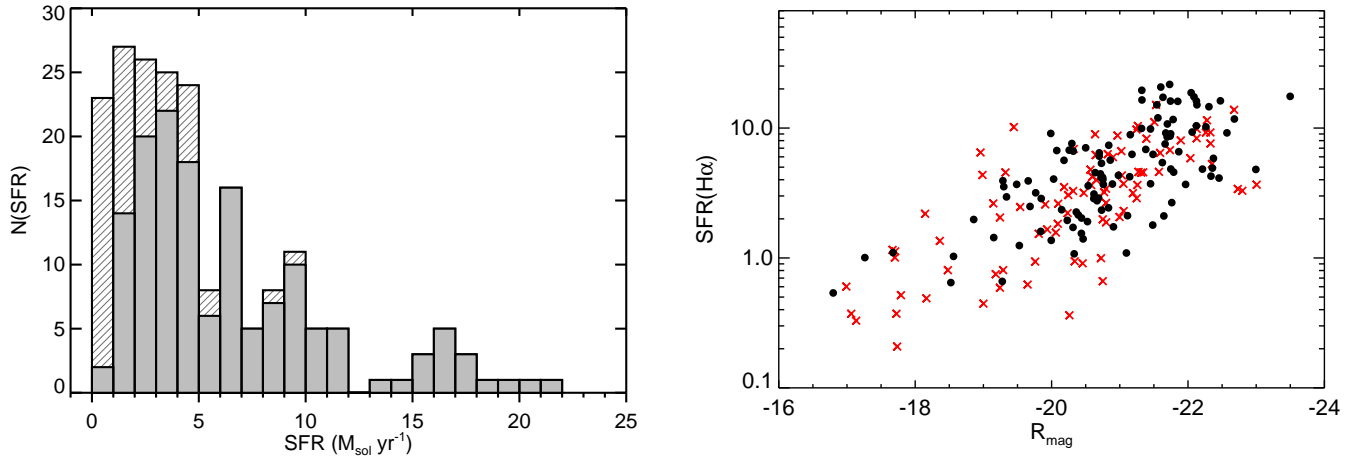


FIG. 11.— *Left*— Observed star formation rate distribution of our $H\alpha$ emitters. The $H\alpha$ flux is reduced to account for 20% of $[N II]$ contamination and converted to SFR using Kennicutt (1998) relation. The sample is split into high- z (shaded area) and low- z (hatched) sub-samples, where the separation between the two categories is $z=0.675$. *Right*— SFR as a function of absolute R-band magnitude derived from F110W and F140W photometry for $H\alpha$ emission below and above 1.25 microns respectively. Black points represent confirmed $H\alpha$ emitters and red crosses the single-line galaxies.

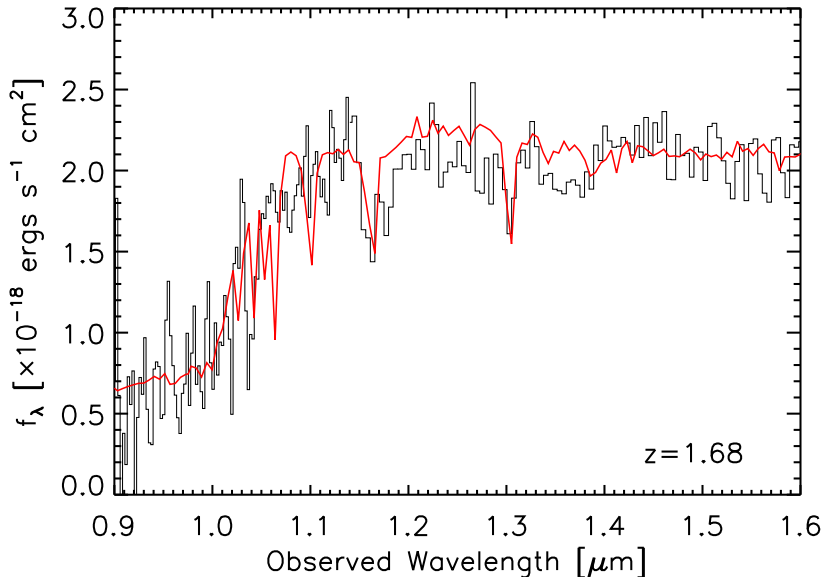


FIG. 12.— Example V: Spectrum of a post-starburst galaxy at $z = 1.68$. A clear Balmer break can be seen in the G102 spectrum between $1.0 < \lambda < 1.1\mu\text{m}$ as well as Balmer absorption lines in the G141 spectrum at 1.17 and 1.3 μm . Plotted (in red) is a Bruzual & Charlot (2003) stellar population model with an age of 600 Myr (e-folding time of 100 Myr), $A_V = 1.2$ mags (assuming a Calzetti reddening curve), and a Salpeter IMF.

While wide-field narrow-band imaging surveys from the ground (e.g. Sobral et al. 2009; Momcheva et al. 2010) yield samples of $\text{H}\alpha$ emitters that are larger than ours and near-IR slit spectroscopy of selected targets can yield emission-line ratios to faint levels (e.g. Pettini et al. 2001), the WFC3 grisms offer a unique opportunity to obtain continuous spectral coverage in the $0.8 - 1.7\mu\text{m}$ region with high sensitivity. Our early results show that we can identify star forming galaxies with space densities comparable to, or larger than, those identified with color selection techniques (e.g. BM/BX or LBG selection; Adelberger et al. 2004) to similar star formation rate thresholds (Shapley et al. 2005, Erb et al. 2006). The typical emission-line galaxy at $z > 1.3$ in our sample has strong $[\text{O III}]5007,4959$ emission and a large $[\text{O III}]/\text{H}\beta$ ratio, similar to the ratios seen in the small number of LBGs at $z > 1.5$ with rest-frame optical spectra (Pettini et al. 2001, Teplitz et al. 2000, Lemoine-Busserolle et al. 2003, Maiolino et al. 2008, Hainline et al. 2009). Coupled with the high $[\text{O III}]/\text{H}\alpha$ ratio and weak $[\text{O II}]3727$ these suggest low metal abundances. Future papers from our survey will examine line ratios and their implications for abundances and ionization sources. With the support of our ongoing ground-based, follow-up observing programs, we will be able to measure the mass-metallicity relation at crucial intermediate redshifts, to derive the $\text{H}\alpha$ luminosity function at different redshifts and to study the evolution of the star formation rate density.

Many of our fields contain emission-line objects with extremely high equivalent widths (cf. Figure 9). These strongly star forming emission-line dominated objects are reminiscent of the ultra-strong emission-line (USEL) galaxies at $0 < z < 1$ discovered by Kakazu et al. (2007) (see also Hu et al. 2009) and the “green pea” galaxies found in SDSS by Cardamone et al. (2009). These objects have metallicities comparable to the lowest observed in local sources and may be dwarf galaxies undergoing

their first major star formation episode.

The sensitivity and resolution of the G102 grism also provide the opportunity to search for $\text{Ly}\alpha$ emission lines in addition to the rest-frame optical emission lines discussed here. We have excluded such analysis from the present paper given the limitations of the initial, visual selection of faint emission lines. After further analysis, WFC3 will offer a significant new approach to high-redshift ($z > 6$) searches for $\text{Ly}\alpha$. Though extensive ground-based narrowband searches for $\text{Ly}\alpha$ -emitters have been performed up to $z = 7$, with the most distant confirmed source at $z = 6.96$ (Iye et al. 2006), it is difficult beyond this redshift to find wavelengths with both high sky transmission and low sky emission. Thus, many surveys are limited to a very small range at $z = 7.7$ or $z = 8.8$ (e.g. Sobral et al. 2009), without any reliable $\text{Ly}\alpha$ emission-line candidates.

In addition to the WISP survey, two large observing programs with the WFC3 grisms will contribute significant results. First, a G141 survey of the GOODS North fields is underway (GO-11600; PI=Weiner), reaching depths comparable or slightly better than WISP. Secondly, the CANDELS multi-cycle treasury program (GO-12060 through 12064; PI=Faber and Ferguson) will obtain deep spectroscopy of selected pointings targeted to follow-up supernovae found in direct imaging. The WISP survey has some limitations compared to these programs due to the parallel mode, including the lack of dithering, but our first analysis demonstrates the great efficiency of this use of the telescope. WFC3 parallels can obtain large spectroscopic samples of emission-line objects during the peak epoch of star formation, free from the most common selection biases.

We gratefully acknowledge the dedicated efforts of several staff members at the Space Telescope Institute to make the new Grism Parallel observations as successful

as possible. In particular, we thank Galina Soutchkova, Iain Neill Reid, Larry Petro, Karla Peterson, Denise Taylor, Kenneth Sembach, Bill Workman, Claus Leitherer, John MacKenty, Howard Bushouse, Ron Downes and Alan Patterson. We thank the ST-ECF team of Martin

Kümmel, Harald Kuntschner and Jeremy Walsh for their help with the data reduction and spectrum extraction processes and advice about the WFC3 calibration status. We also acknowledge the important contributions to supporting parallel observations by the late Roger Doxey.

REFERENCES

- Abraham, R. G. et al. 2004, *ApJ*, 127, 2455
 Bell, E. F., McIntosh, D. H., Katz, N., & Weinberg, M. D. 2003, *ApJS*, 149, 289
 Bertin, E., & Arnouts, S. 1996, *A&AS*, 117, 393
 Bunker, A. J., Warren, S. J., Hewett, P. C., & Clements, D. L. 1995, *MNRAS*, 273, 513
 Chen, H.-W., et al. 2003, *ApJ*, 586, 745
 Cimatti, A., et al. 2004, *Nature*, 430, 184
 Colbert, J. W., Malkan, M. A., & Rich, R. M. 2006, *ApJ*, 648, 250
 Daddi, E., et al. 2007, *ApJ*, 670, 156
 Daddi, E., et al. 2005, *ApJ*, 626, 680
 Doherty, M., Bunker, A. J., Ellis, R. S., & McCarthy, P. J. 2005, *MNRAS*, 361, 525
 Doherty, M., Bunker, A., Sharp, R., Dalton, G., Parry, I., Lewis, I. 2006, *MNRAS*, 370, 331
 Drozdovsky, I., Yan, L., Chen, H.-W., Stern, D., Kennicutt, R., Jr., Spinrad, H., & Dawson, S. 2005, *AJ*, 130, 1324
 Erb, D., Shapley, A., Pettini, M., Steidel, C., Reddy, N., Adelberger, K. 2006, *ApJ*, 644, 813
 Faber, S. M., et al. 2007, *ApJ*, 665, 265
 Freudling, W., Kümmel, M., Haase, J., Hook, R., Kuntschner, H., Lombardi, M., Micol, A., Stoehr, F., Walsh, J. 2008, *A&A*, 490, 1165
 Gallego, J., Zamorano, J., Rego, M., Alonso, O., & Vitorres, A. G. 1996, *A&AS*, 120, 323
 Gardner, J. P., et al. 1998, *ApJ*, 492, L99
 Hainline, K. N., Shapley, A. E., Kornei, K. A., Pettini, M., Buckley-Geer, E., Allam, S. S., & Tucker, D. L. 2009, *ApJ*, 701, 52
 Hicks, E. K. S., Malkan, M. A., Teplitz, H. I., McCarthy, P. J., & Yan, L. 2002, *ApJ*, 581, 205
 Hopkins, A. M., Connolly, A. J., & Szalay, A. S. 2000, *AJ*, 120, 2843
 Hopkins, A. M., 2000, *ApJ*, 615, 209
 Hu, E. M., Cowie, L. L., Kakazu, Y., Barger, A. J. 2009, *ApJ*, 698, 2014
 Iye, M., et al. 2006, *Nature*, 443, 186
 Kakazu, Y., Cowie, L. L., Hu, E. M. 2007, *ApJ*, 668, 853
 Kennicutt, R. C., Jr. 1998, *ARA&A*, 36, 189
 Kimble, R. A., MacKenty, J. W., O'Connell, R. W., & Townsend, J. A. 2008, *Proc. SPIE*, 7010,
 Kriek, M., et al. 2008, *ApJ*, 677, 219
 Koekemoer, A. M., Fruchter, A. S., Hook, R. N., Hack, W. 2002, *The 2002 HST Calibration Workshop: Hubble after the Installation of the ACS and the NICMOS Cooling System*, ed. S. Arribas, A. Koekemoer, & B. Whitmore (Baltimore, MD: STScI), 337
 Kuemmel, M., Walsh, J. R., Pirzkal, N., Kuntschner, H., Pasquali, A. 2009, *PASP*, 121, 59
 Kuemmel, M., Kuntschner, H., Walsh, J. R., Lombardi, M., Stoehr, F., Haase, J., Hook, R. N., Rosati, P., Micol, A., Fosbury, R., Freudling, W. 2009, *ASPC*, 411, 430
 ST-ECF ISR WFC3-2009-18 WFC3 SMOV proposal 11552: Calibration of the G102 grism H. Kuntschner, H. Bushouse, M. Kuemmel, J. R. Walsh
 ST-ECF ISR WFC3-2009-17 WFC3 SMOV proposal 11552: Calibration of the G141 grism H. Kuntschner, H. Bushouse, M. Kuemmel, J. R. Walsh.
 Le Fevre, O., Crampton, D., Lilly, S. J., Hammer, F., Tresse, L. 1995, *ApJ*, 455, 60
 Lemoine-Busserolle, M., Contini, T., Pelló, R., Le Borgne, J.-F., Kneib, J.-P., & Lidman, C. 2003, *A&A*, 397, 839
 Maiolino, R., et al. 2008, *A&A*, 488, 463
 Malhotra, S., et al. 2005, *ApJ*, 626, 666
 Malkan, M., Teplitz, H., McLean, I. 1996, *ApJL*, 468, 9
 McCarthy, P., Yan, L., Freudling, W., Teplitz, H., Malumuth, E., Weymann, R., Malkan, M., Fosbury, R., Gardner, J., Storrie-Lombardi, L., Thompson, R., Williams, R., Heap, S. 1999, *ApJ*, 520, 548
 McCarthy, P. J., et al. 2004, *ApJ*, 614, L9
 Momcheva, I., Lee, J., Ly, C., Salim, S., Dale, D., Garcia, C., Finn, R., Ouchi, M. 2010, *BAAS*, 21506806
 Pasquali, A., et al. 2006, *ApJ*, 636, 115
 Pettini, M., Shapley, A. E., Steidel, C. C., Cuby, J.-G., Dickinson, M., Moorwood, A. F. M., Adelberger, K. L., & Giavalisco, M. 2001, *ApJ*, 554, 981
 Pirzkal, N., Xu, C., Malhotra, S., et al. 2004, *ApJS*, 154, 501
 Pirzkal, N., Malhotra, S., Rhoads, J. E., Xu, C. 2007, *ApJ*, 667, 49
 Rhoads, J. E., et al. 2005, *ApJ*, 621, 582
 Savaglio, S., Glazebrook, K., Le Borgne, D., Juneau, S., Abraham, R. G., Chen, H.-W., Crampton, D., McCarthy, P. J., Carlberg, R. G., Marzke, R. O., Roth, K., Jrgensen, I., Murowinski, R. 2005, *ApJ*, 635, 260
 Shapley, A. E., Steidel, C. C., Adelberger, K. L., Dickinson, M., Giavalisco, M., & Pettini, M. 2001, *ApJ*, 562, 95
 Shapley, A. E., Coil, A. L., Ma, C.-P., & Bundy, K. 2005, *ApJ*, 635, 1006
 Shim, H., Colbert, J., Teplitz, H., Henry, A., Malkan, M., McCarthy, P., Yan, L. 2009, *ApJ*, 696, 785
 Sobral, D., et al. 2009, *MNRAS*, 398, 75
 Straughn, A. N., et al. 2008, *AJ*, 135, 1624
 Straughn, A. N., et al. 2009, *AJ*, 138, 1022
 Teplitz, H., Malkan, M., and McLean, I. 1999, *ApJ*, 514, 33
 Teplitz, H. I., et al. 2000, *ApJ*, 533, L65
 Teplitz, H. I., Collins, N. R., Gardner, J. P., Hill, R. S., Heap, S. R., Lindler, D. J., Rhodes, J., & Woodgate, B. E. 2003, *ApJS*, 146, 209
 Teplitz, H. I., Collins, N. R., Gardner, J. P., Hill, R. S., & Rhodes, J. 2003, *ApJ*, 589, 704
 van der Werf, P. P., Moorwood, A. F. M., & Bremer, M. N. 2000, *A&A*, 362, 509
 van Dokkum, P.G., Brammer, G. 2010, arXiv:1003.3446
 Yan, L., McCarthy, P., Freudling, W., Teplitz, H., Malumuth, E., Weymann, R., Malkan, M. 1999, *ApJ*, 519, 47
 Yan, L., McCarthy, P., Weymann, R., Malkan, M., Teplitz, H., Storrie-Lombardi, L., Smith, M., Dressler, A. 2000, *AJ*, 120, 575